Cooperative Binding of Cytosolic Type III Secretion System Proteins to the Injectisome Revealed by Live-Cell Single-Molecule Localization Microscopy

Olivia I.C. de Cuba[1], Gopika A. Lekshmi[2], Caroline F. Tyndall[2], Andreas Gahlmann[1,3,4,#]

[1] Department of Molecular Physiology & Biological Physics, University of Virginia School of Medicine, Charlottesville, Virginia.

[2] Department of Biology, University of Virginia, Charlottesville, Virginia.

[3] Department of Chemistry, University of Virginia, Charlottesville, Virginia.

[4] Department of Biomolecular Engineering, University of Virginia, Charlottesville, Virginia.

[#] Address correspondence to agahlmann@virginia.edu

ABSTRACT

Type III secretion systems (T3SSs) are employed by many Gram-negative bacteria to translocate virulent effector proteins into host cells. Secretion occurs through the T3SS injectisome, a multi-membrane-spanning biomolecular machine. While the overall structure of the injectisome is becoming increasingly well defined, the structural dynamics that regulate secretion remain unresolved. Particularly important for the functional regulation of type 3 secretion are the cytosolic injectisome proteins which transiently associate with injectisomes and whose structural dynamics and function remain incompletely understood. Here, we use long-exposure single-molecule localization microscopy to quantify the bound times of the cytosolic components SctQ, SctL, and SctN, at the injectisome of *Yersinia enterocolitica* both in controllably induced secretion ON and OFF states and in the presence and absence of effector proteins. In the absence of effector proteins, each component exhibits distinct short-lived binding behavior on a timescale of seconds. However, the presence of the effector protein YopE increases bound times and synchronizes binding behavior across components, specifically without active secretion. Upon activation of secretion, a subpopulation of long-lived binding events emerges for SctQ, SctL, and SctN even within the same injectisomes, indicating that binding behavior between these proteins is secretion state-dependent and cooperative. These findings establish that the interaction kinetics between cytosolic injectisome proteins are modulated by the presence of secretion substrates *and* secretion activating signals, and reveal a new layer of heterogeneity in the functional regulation of type 3 secretion.

38 **INTRODUCTION**

39 Type III secretion systems (T3SSs) are conserved multi-membrane spanning protein
40 complexes used by many Gram-negative pathogens to assemble either flagella or
41 injectisomes that translocate effector proteins directly into eukaryotic cells[1]. The
42 injectisome includes an extracellular needle connected through the bacterial envelope to a
43 membrane-embedded export apparatus and a cytosolic protein complex that engages,
44 energizes, and prioritizes effector proteins for secretion (Fig. 1a)[2-5].

45 The biogenesis of the T3SS follows a hierarchical process in which substrates are
46 secreted in a defined order to assemble the functional injectisome and subsequently
47 secrete effector proteins. Early substrates, such as the inner rod (SctI) and needle protein
48 (SctF), are secreted first to assemble the needle structure[6,7]. This enables secretion of
49 middle substrates, the translocator proteins (SctA, SctB, SctE), which form the translocon
50 pore in the host membrane[8]. Once this pore is established, the system switches to
51 secreting late substrates, the effector proteins, directly into the host cell. These transitions
52 are controlled by molecular switches: the ruler protein SctP and export gate component
53 SctU halt early substrate secretion once the needle reaches its final length, while the
54 gatekeeper complex (SctW) dissociates from SctV to regulate the shift from translocator to
55 effector secretion[9,10]. In *Yersinia enterocolitica*, an assembled injectisome can be reversibly
56 turned ON and OFF using the calcium switch; high calcium represses secretion, while
57 calcium depletion activates effector secretion[11-13]. While the cytosolic components play a
58 role in the secretion of early, middle and late substrates, if and how the cytosolic

59 components of the injectisome reorganize to accommodate these functional transitions is
60 not yet fully understood.

61 *In situ* structural studies by cryo-electron tomography have converged on an
62 architectural model in which the export apparatus is capped on its cytosolic face by a
63 multiprotein assembly comprising SctK, SctQ, and SctL, arranged around the hexameric
64 ATPase SctN and its central stalk (SctO)[2,3,14,15]. Initial *in situ* observations using *Shigella* and
65 *Salmonella* minicell-producing mutants revealed six distinct cytoplasmic "pods" that
66 tether SctN to the membrane-embedded SctD ring[2,16,17]. In contrast, in *Yersinia* a more
67 continuous, ring-like density beneath the injectisome, reminiscent of the flagellar C ring,
68 was observed[18,19]. These densities include SctK, SctQ, and likely $SctQ_C$, the alternatively
69 expressed C-terminal fragment of SctQ[20,21], while SctL retains a six-fold symmetric spoke-
70 like arrangement cradling SctN. Protein-protein interaction studies using bacterial hybrid
71 systems[22-24] and photo-crosslinking[25] have mapped a sequential SctK–Q–L–N arrangement,
72 with SctQ playing a particularly enigmatic role; its N-terminal domain has been implicated
73 in interactions with SctK[25], $SctQ_C$[26], SctN[23], SctD[27], and even chaperone-effector
74 complexes[23,24,28]. Together, these findings provide useful information about which proteins
75 interact at the injectisome, but they offer limited insight into how these proteins (re-
76)organize in response to environmental cues.

77 Structural and mutational analyses have begun to define how SctQ, SctL, and SctN
78 interact within this cytosolic assembly. Studies in *Salmonella* and *Shigella* demonstrate
79 that the ATPase SctN uses a short N-terminal hook to bind a dimer of SctL, and that
80 deletion of this N terminal domain disrupts both ATPase oligomerization and secretion[23,29].

81 SctL is organized into two functional regions, with a C-terminal segment (~140-220) that
82 interacts with SctN and an N-terminal adaptor domain (residues 1-30) that contacts C-
83 terminal SctQ (SPOA) domains[22,26]. Within this N-terminal adaptor segment, a conserved
84 hydrophobic triad mediates contacts with complementary grooves on the two C-terminal
85 (SPOA) folds of SctQ[26]. In addition to these SPOA-mediated interactions, SctQ interacts
86 with SctK through its N-terminal region[26]. Finally, electrostatic interactions between SctK
87 and SctD dock the cytosolic complex proteins to the membrane[30]. SctD is an integral
88 membrane ring protein with a transmembrane domain anchoring the injectisome and a
89 cytosolic domain that interacts with SctK[31]. These interactions, supported by cryo-electron
90 tomography and crosslinking studies, reinforce the sequential SctK–Q–L–N arrangement
91 that bridges the export apparatus to the ATPase[2,25,32]. Mutations disrupting either the C-
92 terminal (SPOA) interfaces of SctQ or the adaptor motif of SctL destabilize cytosolic
93 complex assembly and abolish secretion[26,32]. These domains constitute the structural core
94 architecture that underlies the (cooperative) binding kinetics examined in this study.

95 Complementing these structural insights, biochemical and genetic studies have
96 illuminated a functional role for the cytosolic injectisome proteins in substrate secretion
97 hierarchy. A high molecular weight complex comprising SctK, SctQ, and SctL was shown to
98 coordinate the sequential loading of translocases (which form the translocon pore) and
99 effector proteins, each guided by cognate chaperones[33]. Using native gel electrophoresis
100 and subcellular fractionation in *Salmonella*, this study demonstrated that this so-called
101 "sorting platform complex" remains intact even in the absence of the needle complex,
102 suggesting it assembles independently and may serve as a pre-assembled substrate

103 queue. Disruption of this sorting platform complex impairs secretion efficiency and
104 abolishes substrate prioritization, underscoring the regulatory importance of this cytosolic
105 interface[33]. Whether similar organizational principles apply across species remains to be
106 determined. Together, these studies define the components and functional organization of
107 the cytosolic interface, but they provide limited insight into how these proteins dynamically
108 bind and unbind from the injectisome.

109 Fluorescence-recovery-after-photobleaching (FRAP) experiments in living cells have
110 shown that the cytosolic interface of the injectisome is highly dynamic. In *Yersinia*, SctQ
111 exchanges between injectisome-bound and cytosolic pools with a recovery half-time of
112 roughly one minute, accelerating under secreting conditions and requiring ATPase activity,
113 as recovery is abolished when ATPase function is (genetically) disrupted[34]. These data
114 indicate that SctQ binding and unbinding is connected to secretion activity. Single-
115 molecule tracking by our lab and others, in *Y. enterocolitica* subsequently revealed that
116 SctQ, SctL, and SctN populate multiple diffusive states in addition to an injectisome-
117 bound state[28,35,36]. These data are consistent with the formation of hetero-oligomeric
118 complexes that assemble in the cytosol and remain stable for at least several hundreds of
119 milliseconds and possibly longer. A recent study suggested that chaperones facilitate a
120 cytosolic handover of effector proteins to cytosolic SctQ-containing complexes[37]. These
121 SctQ- and effector-containing complexes were proposed to shuttle substrates to the
122 injectisome, implying that substrate availability informs both the composition of cytosolic
123 complexes and their binding to the injectisome[28,37,38]. Together, these observations suggest

124 a dynamic picture in which cytosolic complex formation, substrate loading, and
125 injectisome engagement are kinetically coupled.

126 Here, we use long-exposure single-molecule localization microscopy to extract the
127 bound-time distributions (also referred to as residence times) of SctQ, SctL, and SctN at
128 the injectisome of *Y. enterocolitica* in effector-free and YopE-expressing backgrounds as
129 well as under secretion ON and OFF conditions. We also utilize 3D single-molecule
130 tracking to quantify the bound fraction of SctQ as a proxy for the binding rate k_{on} under
131 different secretion states and the presence/absence of YopE. This approach allows us to
132 test whether secretion state and effector presence differentially regulate the binding
133 kinetics and the number of resolvable bound state time constants. By quantifying kinetic
134 parameters across defined environmental and substrate conditions, we provide new
135 insights into how the T3SS cytosolic proteins dynamically adjust their interactions with
136 injectisomes in response to secretion activating signals and secretion substrate
137 availability.

138 **RESULTS**

139 To quantify the bound times of cytosolic T3SS components at the injectisome, we
140 used a biosafety level 1-compatible *Yersinia enterocolitica* strain lacking six major effector
141 proteins referred to as $T3SS^{\Delta effector}$ (also known as IML421asd, see Methods, list of strains)[4].
142 We expressed Halo-tagged SctQ and SctL from their native loci via allelic exchange; Halo-
143 SctN was expressed from a plasmid due to unsuccessful allelic replacement attempts. All
144 fusion proteins were confirmed to be stable (Fig. S1a) and functional (Fig S1b), i.e. capable
145 of reversible induction of secretion by the calcium effect (Fig S1c). These strains thus
146 allowed us to probe the binding behavior of SctQ, SctL, and SctN in the absence of effector
147 proteins.

148 A small fraction of Halo-fusion proteins (1-5 per cell) was visualized using low
149 concentrations of dye coupled with long-exposure time imaging. Under these conditions,
150 fast-moving molecules blur into the background, and stationary, injectisome-bound
151 proteins are detected as sharp point spread functions (Fig 1b). The pooled bound times
152 were displayed as probability density function (pdf)-normalized histograms and fit with
153 single- or bi-exponential decays. The resulting bound time constant, τ, is the inverse of the
154 dissociation rate of the respective protein from the injectisome, k_{off}.

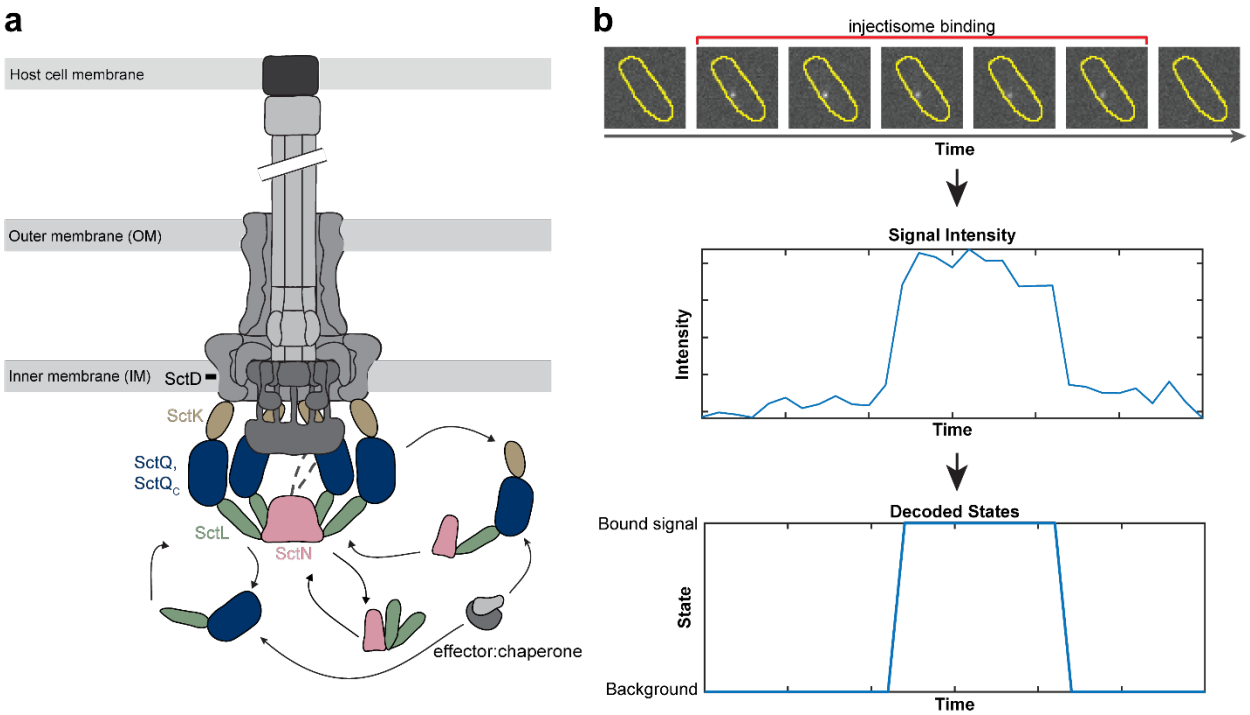

Figure 1: (a) Schematic of the Type III Secretion System (T3SS) architecture in *Yersinia enterocolitica*, highlighting the substructures and the cytosolic components analyzed in this study: SctQ, SctL, and SctN. The stoichiometry of these proteins at the injectisome have been estimated previously at 24 copies of SctQ[39], 12 copies of SctL[39], and 6 copies of SctN[40]. **(b)** Long-exposure imaging strategy used to extract bound times from stationary single-molecules. Injectisome-bound molecules appear as sharp foci, while cytosolic diffusing molecules blur into the background. A hidden-Markov model helps distinguish between the bound signal and background state, enabling an automated transition from signal intensities to decoded states used to measure bound times at individual injectisomes (see text for details).

Effector-Free Conditions Reveal Distinct Binding Dynamics for Injectisome-Associated Proteins SctQ, SctL, and SctN

In the T3SS$^{\Delta effector/OFF}$ condition, the bound time histograms of SctQ, SctL and SctN are best fit by single exponential decays (Fig. 2a-c). Notably, all three proteins exhibit bound times on the order of a few seconds, but the fitted bound time constants are all distinct. SctQ exhibits the shortest bound time constant, τ = 2.5 s [2.4, 2.5], while the bound times constant of SctL and SctN are slightly longer, τ = 3.4 s [3.3, 3.4] and τ = 3.0 s [2.9, 3.0], respectively (the square brackets represent the 99% confidence intervals).

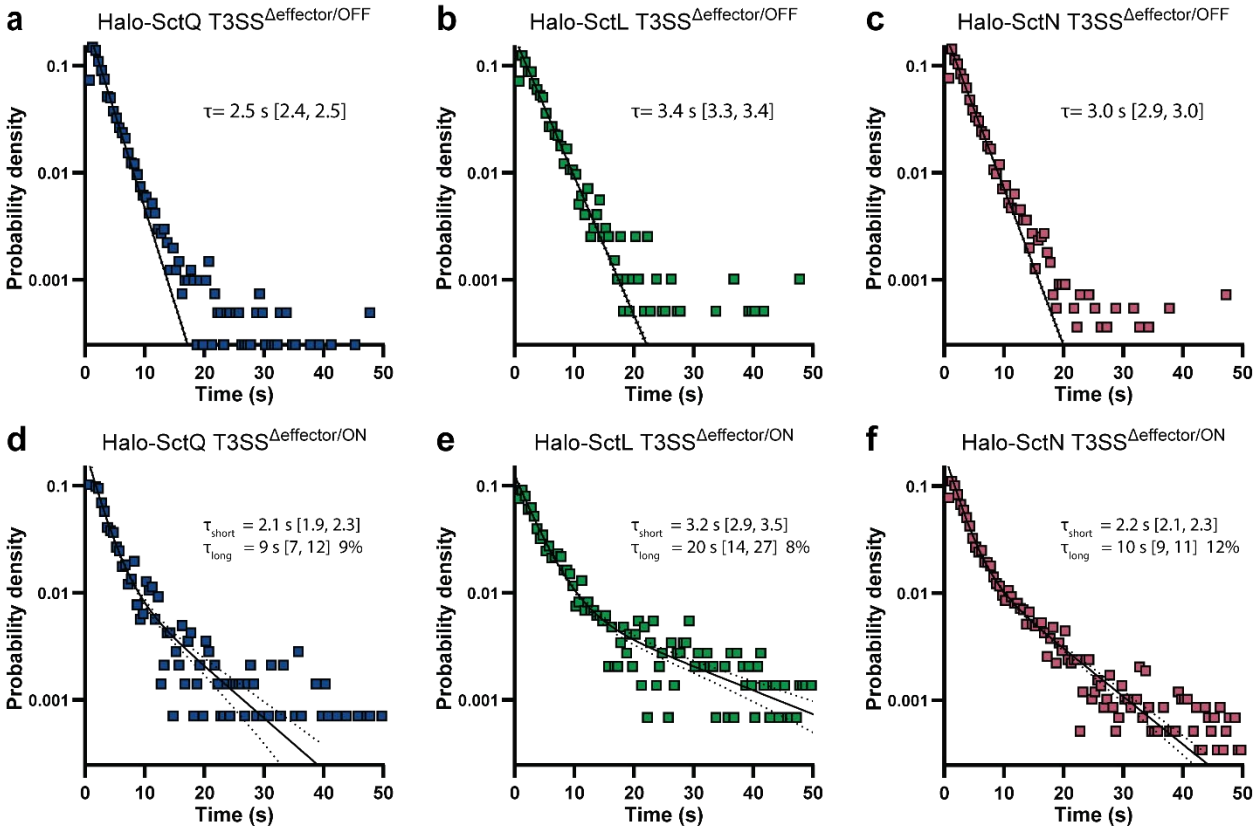

Figure 2: Distinct bound times for SctQ, SctL, and SctN and emergence of long-lived binding events under secretion ON conditions. Bound time distributions for Halo-tagged SctQ, SctL, and SctN under secretion OFF (top row) and ON (bottom row) conditions in the effector-free background. **(a–c)** Under secretion OFF conditions, all three proteins exhibit mono-exponential decay kinetics with distinct bound times: SctQ (τ = 2.5 s), SctL (τ = 3.4 s), and SctN (τ = 3.0 s). **(d–f)** Under secretion ON conditions, a subpopulation of long-lived binding events emerges for all proteins, requiring bi-exponential fits. Long-lived events comprise 9% (SctQ), 8% (SctL), and 12% (SctN) of trajectories, indicating two binding states at the injectisome. The total counts for the histograms in a-f are *n* = 4063, *n* = 1973, *n* = 5545, *n* = 1417, *n* = 1463, and *n* = 5857, respectively.

Under secretion ON conditions, we observed a stark change in the binding behavior of SctQ, SctL, and SctN at the injectisome. Rather than a simple difference in bound time constant, the single-molecule bound time data revealed a subpopulation of binding events with substantially longer durations (>10 s), necessitating bi-exponential fits to the bound time distributions. These long-lived events comprised approximately 9% of SctQ, 8% of SctL, and 12% of SctN trajectories (Fig. 2d-f), indicating the emergence of a distinct and

189 more long-lived binding mode at the injectisome. The finding of long-lived states across all
190 three proteins points to a coordinated and potentially cooperative injectisome-bound
191 configuration under secretion ON conditions.

192 Notably, the short component of the bi-exponential fit was shorter under ON than
193 OFF conditions: for example, SctQ's short-term bound time decreased from 2.5 s (OFF) to
194 2.1 s (ON). When considering both short- and long-lived events, the weighted average
195 bound time constants were 2.7 s for SctQ, 4.4 s for SctL, and 3.1 s for SctN under
196 $T3SS^{\Delta effector/ON}$ conditions. Thus, despite the prevalence of shorter short-lived events in our
197 single-molecule data, the bound times constant did not skew toward faster exchange
198 overall under secreting conditions, as previously reported using FRAP[34]. Because FRAP
199 half-times average over relatively few individual injectisomes, we asked whether individual
200 injectisomes engage in both short- and long-lived binding, or whether distinct classes of
201 injectisomes exhibit either short or long-lived binding modes only.

202

203 **The Same Injectisome Can Engage in Short and Long Binding Modes**

204 Within the same bacterial cell, we observed both short- and long-lived binding
205 events for SctQ, SctL, and SctN (Fig. 3a), establishing that the emergence of long-lived
206 states is not due to cell-to-cell variation. This observation is possible because each single-
207 molecule binding event can be localized to a specific cell and even to a specific subcellular
208 location (Fig. 1b) and repeated binding events at the same spatial locations, i.e. clusters of
209 single-molecule localizations, can be used to approximate the position of injectisomes. To

assess whether long-lived binding events preferentially occur at a distinct subset of injectisomes, we clustered binding events within each field of view using DBSCAN (ε = 150 nm, minPts = 2) and classified events as long if their bound time exceeded 15 seconds. For injectisomes with multiple binding events, we found subsets showing exclusively short-lived events, exclusively long-lived events, as well as mixed duration events (Fig. 3b, table S2).

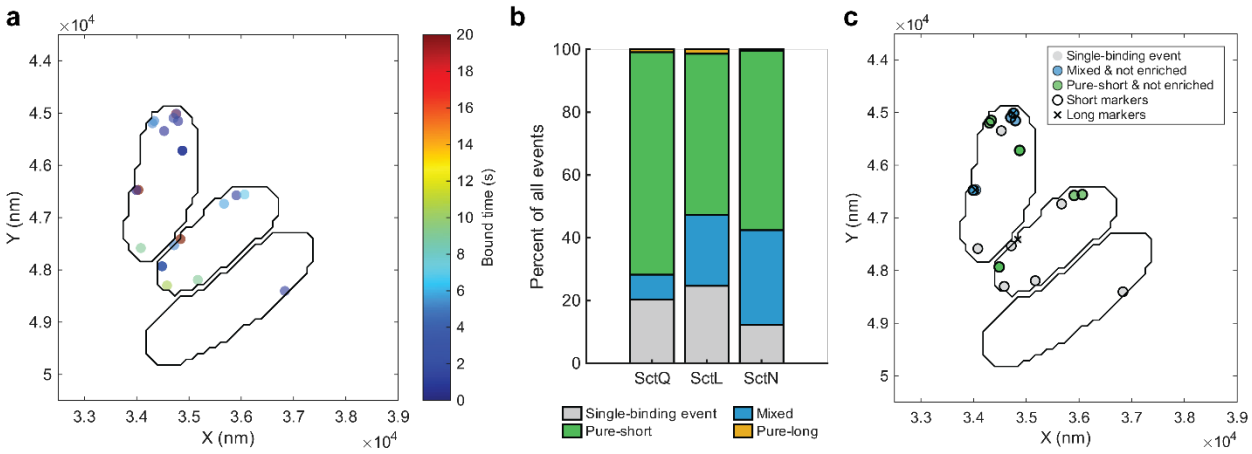

Figure 3: Short- and long-lived binding events occur at the same injectisome. (a) Representative cells showing spatial co-localization of short- and long-lived binding events for SctQ, SctL, and SctN, confirming that both binding modes occur within the same cell and at the same subcellular locations. **(b)** Classification of injectisomes based on binding profiles: mixed (both short and long), short-only, and long-only. (Breakdown of all counts analyzed can be found in Table S2.) **(c)** Statistical analysis using a hypergeometric test with FDR correction (ε = 100 nm, minPts = 2; long = dwell ≥ 30 frames) reveals no significant enrichment of long-lived events at specific clusters, indicating that binding mode heterogeneity is not spatially segregated.

We note that these data were obtained by sparsely labeling the proteins of interest. The abovementioned injectisome classification could therefore be skewed because we are not sampling all the possible binding events at a given injectisome. We therefore compared the observed fraction of long events within clusters to the global fraction of long events across the field of view. Using a hypergeometric test with Benjamini–Hochberg correction (α =

230 0.05), we asked whether clusters contained more long-bound events than expected under
231 random distribution. No clusters showed significant enrichment of long events for any
232 protein, indicating that long-bound events were not spatially localized beyond random
233 expectation. We repeated this analysis for short-bound events and again observed no
234 statistical evidence for enrichment. Based on this analysis, we conclude that long- and
235 short- lived bound states are not spatially segregated and occur at the same injectisome
236 during the 22-min time windows of data acquisition.

237

238 **YopE Modulates Injectisome Binding Dynamics, With SctQ Showing Distinct**
239 **Sensitivity Across Secretion States**

240 To determine how the presence of effector proteins influences injectisome-
241 associated protein dynamics, we quantified the bound lifetimes of SctQ, SctL, and SctN
242 under secretion ON and OFF conditions in the presence of the effector protein YopE. YopE
243 was constitutively expressed from a plasmid and confirmed to be successfully secreted in
244 a Ca^{2+}-dependent manner in all strains (Fig S1b). (SycE, the cognate chaperone of YopE is
245 natively expressed from the pYV virulence plasmid in all of the strains used in this study.)

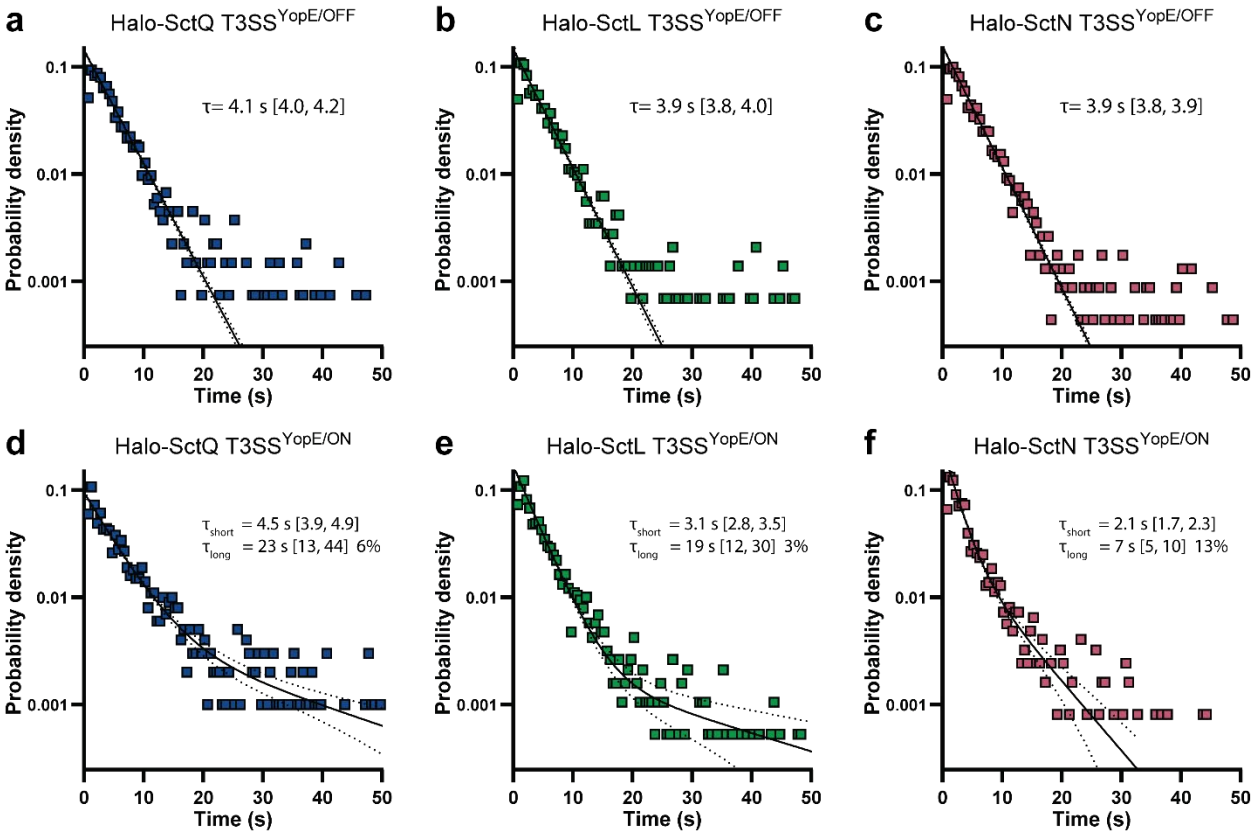

Figure 4: Effector presence increases bound times and synchronizes binding behavior. Bound time distributions for SctQ, SctL, and SctN under secretion OFF (top row) and ON (bottom row) conditions in the presence of the effector protein YopE. **(a–c)** Under secretion OFF conditions, all three proteins show increased bound times compared to the effector-free background, with mono-exponential fits yielding τ ≈ 4 s for all proteins. **(d–f)** Under secretion ON conditions, SctQ exhibits both an increased short bound time (τ = 4.5 s) and a distinct long-lived subpopulation (τ = 23 s, 6% of events). SctL and SctN show smaller changes, indicating component-specific sensitivity to effector presence. The total counts for the histograms in a-f are *n* = 1345, *n* = 1446, *n* = 2292, *n* = 1003, *n* = 1902, and *n* = 1240, respectively.

In the presence of YopE, all three proteins exhibited increased bound times compared to the effector-free condition (T3SS$^{\Delta effector/OFF}$), and their bound time constants converged to statistically indistinguishable values (Fig. 4a-c). Mono-exponential fits yielded bound time constants of τ = 4.1 s [4.0, 4.2] for SctQ, τ = 3.9 s [3.8, 4.0] for SctL, and τ = 3.9 s [3.8, 3.9] for SctN. The increase was most pronounced for SctQ, which nearly doubled its bound time constant relative to the effector-free condition. These findings indicate that effector

262 presence alone can increase the bound time of cytosolic components at the injectisome in
263 secretion OFF conditions.

264 Next, we asked whether these effects persist during active secretion ($T3SS^{YopE/ON}$). As
265 in $T3SS^{\Delta effector/ON}$, the $T3SS^{YopE/ON}$ condition revealed a subpopulation of binding events with
266 substantially longer durations (>10 s), again prompting bi-exponential fits to the bound
267 time distributions. These long-lived events comprised 6% of SctQ, 3% of SctL, and 13% of
268 SctN trajectories (Fig. 4d-f). As before, we observed mixed long- and short-bound behavior
269 at single injectisomes (Table S3) and there was no statistical evidence for enrichment of
270 any one type of binding at specific spatial locations (Fig S3), again ruling out the possibility
271 of two distinct classes of injectisomes. SctQ exhibits the longest short-bound time (τ = 4.5
272 s [3.9, 4.9]), while the short-bound times of SctL and SctN are τ = 3.1 s [2.8, 3.5] and τ = 2.1
273 s [1.7, 2.3], respectively. Thus, the presence of the YopE effector more than doubles the
274 short-bound duration for SctQ, while leaving the short-bound durations for SctL and SctN
275 largely unchanged.

276

277 **SctQ Injectisome-Bound Fraction Is Not Sensitive to Secretion State or YopE Effector**
278 **Presence**

279 The observation that SctQ exhibits slightly longer bound time constants in the
280 secretion ON state does not match previous FRAP measurements that indicate faster
281 protein exchange under secreting conditions[34]. Protein exchange at injectisomes is a
282 function of both the binding rate constant (k_{on}) and the unbinding rate constant (k_{off}). The

283 above bound time measurements only report on the k_{off} and so do not rule out changes in
284 the association rate constant. An increase in k_{on} would increase the fraction of injectisome
285 bound molecules, especially if bound time remains constant or increases. However, all
286 available binding sites at the injectisome may already be occupied or rapidly reoccupied
287 under saturating conditions, in which case we expect bound fraction to remain constant
288 across our experimental conditions.

289 Our previous 3D single-molecule tracking results in *Y. enterocolitica* under secretion
290 ON conditions found freely-diffusing cytosolic states for eYFP-SctQ in addition to a
291 prominent stationary state corresponding to injectisome-bound SctQ[35,36]. Similar results
292 are obtained for Halo-SctQ (Fig. 5a, left panel), under all conditions described above. The
293 fraction of slow-moving SctQ trajectories (mean displacement < 4 nm/ms) thus enables us
294 to estimate the SctQ bound fraction (Fig. 5a, right panel), which may be sensitive to
295 changes in the association rate constant k_{on}. Quantifying the injectisome bound fraction of
296 SctQ using this metric showed very small differences across conditions.

297 To alternatively assess potential variations in injectisome association, we
298 implemented an approach based on the root mean squared (RMS) radius, also called the
299 radius of gyration. This quantifies how spatially spread out the trajectory is around its mean
300 position. For a molecule associated with an injectisome, we expect the trajectory to be
301 spatially confined, with the apparent motion being predominantly due to localization error.
302 When plotting the RMS radius spread for trajectories, we consistently observed a peak
303 below 120 nm and selected this to be the upper threshold for injectisome association
304 (representative cell shown in Fig. 5b). By classifying trajectories below the threshold as

305 injectisome-associated, a bound fraction was computed for the different conditions (Fig.

306 5c). Here too, we found only small variations across our conditions with a series of

307 unpaired t-tests indicated no statistically significant differences (table S5).

308

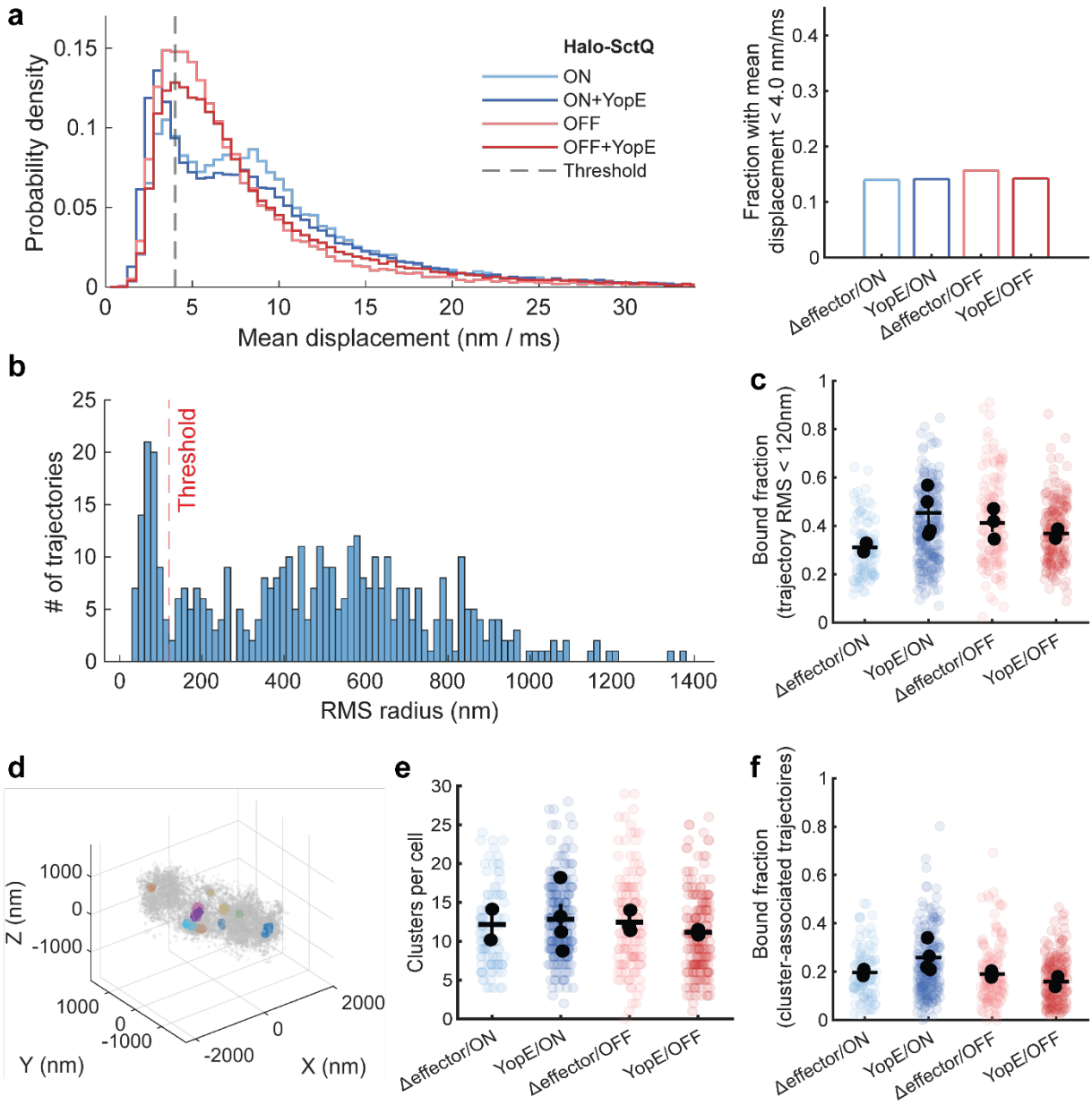

309

310 **Figure 5: SctQ injectisome-bound fraction is not sensitive to secretion state or YopE effector presence.**

311 **(a,** left**)** Pooled single-molecule displacements of Halo-SctQ under four experimental conditions. For each

312 condition, at least 100 cells and 10 000 trajectories were analyzed (see table S4 for exact counts). **(a,** right**)**
313 Quantification of the fraction of slow-moving trajectories (mean displacement < 4 nm/ms) per cell, used as a
314 proxy for injectisome association. **(b)** Histogram of single-molecule trajectory RMS deviations, representative
315 cell, threshold at 120 nm was selected based on tall peak to the left of that threshold, which appears robustly
316 for all cells analyzed. **(c)** RMS threshold-based analysis confirms consistent injectisome-bound fraction
317 across conditions, with minor variation that follows the same patterns as the mean number of injectisomes
318 (see panel e), supporting the conclusion that injectisome bound fraction stays constant across conditions. **(d)**
319 Representative localizations of Halo-SctQ with identified localization clusters: a proxy for injectisomes. **(e)**
320 Number of clusters identified per cell by the clustering analysis of DBSCAN within 60 nm (see methods).
321 Localization clusters are consistent with (repeated) binding to a spatially confined region, i.e. injectisome. The
322 finding of ~12 injectisomes per cell is consistent with previous cellular injectisome counts by other
323 methods[28,41,42]. **(f)** Cluster-based categorization of single-molecule trajectories confirms consistent
324 injectisome-bound fractions across conditions. **(c, e, f)** Bars indicate the mean across biological samples, with
325 error bars representing the standard error of the mean across samples. Colored points show individual cells,
326 while black points denote per-sample means.

327

328 As a third approach, we used spatial clustering of single-molecule localizations. By
329 identifying localization clusters (at the membrane), consistent with injectisome locations
330 (Fig. 5d)[35,36], and classifying single-molecule trajectories as cluster-associated or not, we
331 obtained yet another measure of the injectisome bound fraction (Fig. 5f). Similar to the
332 previous approach, this analysis also revealed that the fraction of cluster-associated
333 trajectories did not change significantly across our experimental conditions, as any
334 observed differences were within statistically expected variation (table S6).

335 Taken together, these data show that the injectisome-bound fraction of SctQ does
336 not vary with secretion state or effector presence. We therefore focus our discussion on the
337 observed changes in injectisome bound times only.

338 **DISCUSSION**

339 During infection, *Yersinia enterocolitica* must rapidly adapt to changing host
340 environments. A rapid transition between the secretion OFF and ON state is thought to be
341 essential for evading immune clearance and thereby persistence at sites of lymphoid
342 colonization[43-47]. Activation of secretion, as well as deactivation, can occur rapidly[47,48] in
343 response to external stimuli, suggesting strong external sensing mechanisms that
344 modulate secretion, possibly through the cytosolic injectisome components.

345 In this study, we measured the bound times of SctQ, SctL, and SctN under secretion
346 OFF and ON conditions in the presence and absence of the effector protein YopE. In
347 secretion OFF conditions, we observed mono-exponential decay kinetics for SctQ, SctL,
348 and SctN, indicating a single, transient bound state at the injectisome for each protein. In
349 the absence of effectors ($T3SS^{\Delta effector}$), each protein exhibited a distinct fitted bound time,
350 with SctQ having the shortest, followed by SctN and SctL, suggesting that these
351 components do not both bind *and* unbind as an assembled unit. Independent exchange of
352 these proteins is a notion additionally supported by a recent study showing that SctQ can
353 still bind to and dissociate from the injectisome even when the inner membrane ring
354 protein SctD is crosslinked and thus unable to exchange itself[49].

355 In contrast, the fitted bound times of all three proteins converged to approximately 4
356 seconds in the presence of the effector protein YopE in the secretion OFF state. This
357 synchronization of bound times shows that effector presence alone, independent of active
358 secretion, can modulate the binding kinetics of cytosolic components. Moreover, this

359 convergence of bound times is consistent with the notion that SctQ, SctL, and SctN both
360 bind and unbind as a part of the same protein complex and is consistent with effector
361 proteins that are preloaded onto cytosolic SctQ-L-N complexes[36,50] that then subsequently
362 bind to injectisomes[37]. Such a mechanism could help prime the system for rapid activation
363 of secretion. The convergence of bound times may reflect a shift toward a more uniform or
364 stabilized interaction mode of SctQ, SctL, and SctN at injectisomes, perhaps due to
365 effector-induced conformational or compositional remodeling. An alternative explanation
366 to intact complex dissociation would be that all other proteins disassemble immediately
367 after at least one of them unbinds from the injectisome. Such a model is supported by gene
368 deletion studies that have established that cytosolic injectisome proteins are mutually
369 dependent on each other injectisome binding[2,32,34,51], expression of each protein is required
370 for injectisome assembly[2,16,52] and type 3 secretion[22-24,29,53]. Regardless of the exact
371 mechanism at play, the continued presence of unsecreted YopE effectors seems to induce
372 a coordinated, bind-and-reject process, where a SctQ-L-N complex binds and unbinds
373 together. Consistent with this interpretation, our data show that such temporally
374 coordinated binding and unbinding indeed disappears in the secretion ON state, in which
375 YopE is secreted and thereby removed from injectisomes.

376 Under secretion ON conditions and irrespective of whether YopE is present, SctQ,
377 SctL, and SctN all display a subpopulation of long-lived binding events, resulting in bi-
378 exponential decay kinetics. Detection of this long-lived bound state is uniquely enabled by
379 single-molecule measurements, which allow direct quantification of injectisome bound
380 times of *individual* protein molecules. Importantly, we observed both short- and long-lived

381 binding events at the same subcellular locations, suggesting that individual injectisomes
382 can engage proteins in different binding modes, one mode being more stable than the
383 other. This raises the intriguing possibility of functional asymmetry within single
384 injectisomes, either through structural heterogeneity within an injectisome or through
385 dynamic switching between distinct operational states in time (our pooled single-molecule
386 data were obtained over a timescale of ~20 minutes). In support of the structural
387 heterogeneity hypothesis, cryoEM studies have shown that the ATPase SctN forms an
388 asymmetric hexamer at the base of the injectisome[54], raising the possibility that asymmetry
389 extends to other cytosolic injectisome components and contributes to the observed kinetic
390 heterogeneity. Future structural and computational studies will be essential to determine
391 whether the short- and long-bound states correspond to distinct conformational or
392 functional states of the injectisome under defined secretion conditions.

393 Among the three cytosolic components analyzed, SctQ consistently exhibited the
394 most pronounced changes in bound time across conditions and was particularly sensitive
395 to the presence of the effector protein YopE. Under secretion OFF conditions, the addition
396 of YopE nearly doubled the SctQ bound time, bringing it into close alignment with SctL and
397 SctN. Under secretion ON conditions, SctQ again showed heightened sensitivity, with both
398 an increased short-bound time and a subpopulation that fits to a longer-bound time
399 constant. This component-specific response supports the notion that SctQ serves in a key
400 regulatory role within the assembled injectisome.

401 Previous studies have examined complete turnover of the SctQ subunits at the
402 injectisome under secretion ON conditions similar to those reported here, as well as a

403 secretion OFF state prior to injectisome assembly[34,49] (which is unlike that reported here).
404 We can also interpret our single molecule bound state lifetimes in the context of complete
405 ring turnover. Assuming 24 SctQ subunits[39] independently exchanging at the observed
406 mixture of lifetimes, the expected time for *all* sites at the injectisome to undergo at least
407 one unbinding event is approximately 21 s under $T3SS^{YopE/ON}$ conditions and 10 s
408 $T3SS^{\Delta effector/ON}$ (see SI for further explanation). Similarly, we estimate approximately 16 s
409 under $T3SS^{YopE/OFF}$ and 10 s for $T3SS^{\Delta effector/OFF}$. FRAP-based measurements of subunit
410 exchange are sensitive to both k_{on} and k_{off}, but are also influenced by additional factors
411 such as photobleaching and binding site occupancy (see SI), which can slow the apparent
412 turnover rate. Taken together, our single-molecule results are qualitatively consistent with
413 previous FRAP observations under similar secretion ON conditions[34,49].

414 Furthermore, our results are compatible with a shuttling model in which SctQ-
415 containing complexes bind effectors, such as YopE, in the cytosol and then deliver the
416 effectors to the injectisome for secretion[37]. We evaluated whether such a mechanism
417 alone could support the total known per-cell secretion rate[55] of 7–60 molecules s^{-1}.
418 Assuming near-saturated occupancy of injectisome binding sites, the fast dissociation rate
419 (derived from τ_{short}) sets an upper bound on secretion throughput. Using the experimentally
420 measured lifetime of Halo–SctQ under $T3SS^{YopE/ON}$ conditions ($\tau \approx 4.5$ s) and an average of
421 12 injectisomes per cell (Fig 5e), predicted secretion rates can reach up to 64
422 molecules s^{-1}(see SI for further explanation). Previously reported secretion fluxes are 7–60
423 molecules s^{-1}, indicating that SctQ shuttling and turnover alone could support effector
424 export even if not every binding event results in a secretion event. We note however that

425 while our results show injectisome-associated dynamics on a timescale compatible with
426 effector translocation, they do not provide direct evidence for an effector shuttling
427 mechanism. Indeed, direct binding of effectors to the injectisome is an alternative and not
428 mutually exclusive mechanism. Future work may be able to distinguish between these
429 mechanisms.

430 In conclusion, our analysis of injectisome-bound lifetimes reveals that cytosolic
431 components exhibit secretion state- and effector-dependent binding modes. In secretion
432 OFF states, distinct bound times for SctQ, SctL, and SctN indicate independent binding
433 and/or unbinding. However, the presence of YopE synchronizes these bound states,
434 consistent with cooperative binding within a SctQ–L–N–YopE complex engaging in a
435 coordinated "bind-and-reject" cycle. Under secretion ON conditions, YopE is secreted and
436 this temporal coordination disappears: biexponential bound time distributions arises as
437 short- and long-bound states manifest at the same injectisome for SctQ, SctL, and SctN.
438 Importantly, comparing effector-free and YopE-expressing strains allowed us to separate
439 the effects of secretion state from those caused by the effector YopE. The fact that
440 cytosolic injectisome protein binding kinetics are altered even in the absence of active
441 secretion supports the idea that cytosolic remodeling, potentially through effector or
442 effector–chaperone interactions, can precondition cytosolic injectisome proteins before
443 injectisome association, and alter their binding behavior at the injectisome. By directly
444 linking effector presence and secretion state to injectisome-bound lifetimes, we show that
445 type 3 secretion does not arise from a static injectisome architecture, but from dynamically
446 changing, cooperative binding kinetics among cytosolic injectisome proteins.

447 **METHODS**

448 **Bacterial culture**

449 *Yersinia enterocolitica* strains were grown overnight in Brain Heart Infusion (BHI, Sigma-
450 Aldrich, St. Louis, MO) media supplemented with nalidixic acid (NaI) (35 µg/mL) and 2,6-
451 diaminopimelic acid (DAP) (80 µg/mL) at 28°C with shaking. Additional antibiotics were
452 included when appropriate: kanamycin (50 µg/mL) and/or chloramphenicol (25 µg/mL). On
453 the day of imaging, overnight culture was back diluted to a target OD_{600} of 0.1-0.3 and
454 grown at 28°C with shaking for 1-1.5 h. For secreting conditions, glycerol (4 mg/mL),
455 $MgCl_2$ (20 mM), and EGTA (5 mM) were then added to the culture, and the culture was
456 transferred to a 37°C water bath or incubator with shaking, for 3h to induce expression of
457 the *yop* regulon and ensure secretion activation. For non-secreting conditions (post-
458 secretion), cells were pelleted by centrifugation at 5,000 × *g* for 3 min and resuspended
459 with fresh BHI supplemented with NaI, DAP, $CaCl_2$ (5 mM) and grown for an additional hour.

460

461 **Strains and Plasmids**

462 Plasmids were constructed using Gibson Assembly. Briefly, DNA fragments with
463 overlapping ends were generated by Q5 PCR (New England Biolabs (NEB), Ipswich, MA) and
464 assembled in a single isothermal reaction. Assembled plasmids were transformed into
465 chemically competent *dh5α E coli* (NEB) and plated on LB agar supplemented with the
466 appropriate antibiotic for selection. Individual colonies were cultured overnight, and
467 plasmid DNA was isolated using a commercial miniprep kit (Qiagen, Hilden, Germany).

468 Plasmid sequences were verified by long-read sequencing (Plasmidsaurus, Eugene, OR).

469 Plasmids were transformed into the appropriate *Yersinia Enterocolitica* strain by

470 electroporation.

471 List of oligonucleotides

Name	Sequence	Used for plasmid
OC116	cacaggaaacacattcaacaatgGCAGAAATCGGTACTGGCTTTCCATTCGACCC	*pAH12::halo-sctN*
OC117	ccgacccacccaattgGCCGGAAATCTCGAGCGTCGACAGCCAG	*pAH12::halo-sctN*
OC118	cattgttgaatgtgtttcctgtgtgggcgcgcc	*pAH12::halo-sctN*
OC119	caattgggtgggtcgggcggct	*pAH12::halo-sctN*
OC163	GTA CCA CGC GGC AGT AAA ATA TCA TCA TTT ATT TCT ACA TCA CTG CCC CTG CCG GC	*pACAC::YopE*
OC164	AGC CTC CAC CTA GCC TTC ACA TCA ATG ACA GTA ATT GCT GCA TCT GTT GCC CC	*pACAC::YopE*

472

473 List of plasmids

Plasmid	Genotype	Reference
1	*pAH12::halo-sctN*	this study
2	*pAH12::halo*	this study
3	*pAH12::mEYFP*	this study
4	*pACAC::YopE*	this study

474

475 List of Strains

Strain	Genotype	Reference
IML421asd (ΔHOPEMTasd)	MRS40 *yopOΔ12-427 yopE21 yopHΔ11-352 yopM23 yopP23 yopT135 Δasd*	[4]
AD4461	IML421*asd halo-sctQ*	[32]
ADTM4525	IML421*asd halo-sctL*	[32]
AD4165	IML421*asd ΔsctN*	[34]

476

477 **Secretion Assay**

478 Cultures were grown as above, to desired secretion state. A small volume of culture was

479 taken to measure the OD_{600}. Main culture was pelleted (20,000 × *g*, 10 min, 4°C) and syringe

480 filtered with a 0.22 µm PVDF filter (Millipore, Burlington, MA). Supernatant was mixed with

481 trichloroacetic acid (TCA) to a final concentration of 10% w/v and incubated overnight at
482 4°C to precipitate proteins within the supernatant. Proteins were collected (20,000 × *g*,
483 20 min, 4°C) and washed with cold acetone (20,000 × *g*, 20 min, 4°C). The pellet was dried
484 at room temperature and resuspended in reducing SDS-PAGE loading buffer (SDS [3%,
485 wt/vol], glycerol [7.5%, wt/vol], 1.5% beta-mercaptoethanol, 0.0125% w/v Coomassie blue,
486 buffered with Tris [37.5 mM]; pH 7.0). Loading volume was normalized across samples ran
487 on the same gel, and proteins were separated by SDS-PAGE on 4–20% polyacrylamide gels
488 (Bio-rad, Hercules, CA). For visualization, the gels were stained with Coomassie Blue and
489 imaged with Bio-rad Gel Doc EZ imager.

490

491 **In-gel fluorescence Assay**

492 Cultures were grown as above, to desired secretion state. HaloTag fusions were incubated
493 with JFX-554 (Promega, Madison, WI) for the last 30 min of culturing. A small volume of
494 culture was taken to measure the OD_{600}. Culture was pelleted (5,000 x *g*, 5 min) and lysed in
495 a buffer of 20 mM Tris HCl, 50 mM NaCl, pH 7.4, supplemented with 0.2 mg/mL of lysozyme
496 and cOmplete™, Mini, EDTA-free Protease Inhibitor Cocktail (Roche, Basel, Switzerland).
497 Samples were resuspended in SDS-PAGE loading buffer and heated for 5 minutes at 98°C
498 before loading. Loading volume was normalized across samples ran on the same gel, and
499 proteins were separated by SDS-PAGE on 4–20% polyacrylamide gels (Bio-rad). For
500 visualization of in-gel JFX-554 fluorescence, a Biorad ChemiDoc MP system was used.

501

502 **Cell Plating for Microscopy**

503 Cultures were grown as described above. In the case of HaloTag visualization, Janelia Fluor
504 HaloTag ligand dye, JFX-554 (Promega) was added to the culture 30 minutes prior to
505 imaging. The appropriate dye concentration was strain dependent: 0.5 nM for Halo-SctQ, 2
506 nM for Halo-SctL, 2nM for Halo-SctN. Cells were pelleted by centrifugation at 5,000 × *g* for
507 3 min and washed three times in fresh M9 minimal media. After the three washes, the
508 remaining pellet was resuspended in M9 supplemented with DAP, $MgCl_2$, glycerol, and
509 EGTA (secreting conditions) or $CaCl_2$. For super-resolution fluorescent imaging, fluorescent
510 fiducial markers (Invitrogen) were added to cell suspensions. Cells were finally plated on
511 1.5% agarose pads in M9 containing DAP and EGTA or $CaCl_2$.

512

513 **Optical Setup**

514 Image data were acquired on a custom-built inverted fluorescence microscope based on
515 the RM21 platform (Mad City Labs, Madison, WI), as previously described[35,56] . Immersion
516 oil was placed between the lens objective (UPLSAPO 100; numerical aperture [NA], 1.4)
517 and the glass coverslip (VWR, Radnor, PA; number 1.5; 22 mm by 22 mm). A 561 nm laser
518 (Coherent, Santa Clara, CA; Genesis MX561-4000 MTM) was used for excitation of JFX-554
519 (Promega Madison, WI) (~600 mW cm^{-2} for single molecule imaging at 25 ms exposure).
520 Zero-order quarter-wave plates (Thorlabs, Newton, NJ, WPQ05M-561) were used to
521 circularly polarize the excitation laser. A dichroic mirror (Chroma zt440/488/561rpc) was
522 used to separate excitation/activation light from fluorescence emission of JFX-554.

523 Fluorescence emission was passed through a filter set including long-pass (514nm), short-
524 pass (800 nm), and notch filter 561 nm/10bp (Semrock, Rochester, NY; LP02-514RU-25,
525 Chroma, Bellows Falls, VT; ET700SP-2P8, and Chroma, Bellows Falls, VT; ZET561NF,
526 respectively). In the case of 3D super-resolution imaging, the emission path contains a
527 wavelength-specific dielectric phase mask (Double Helix, LLC, Boulder, CO) that is placed
528 in the Fourier plane of the microscope to generate a double-helix point spread function
529 (DHPSF)[57,58]. The fluorescence signal is detected on a scientific complementary metal
530 oxide semiconductor (sCMOS) camera (Hamamatsu, Bridgewater, NJ; ORCA-Flash 4.0 V2).
531 A flip mirror in the emission pathway enables toggling the microscope between
532 fluorescence imaging and phase-contrast imaging modes without having to change the
533 lens objective of the microscope. Illumination for phase contrast imaging was achieved
534 with an LED at 625 nm (Thorlabs, Newton NJ; M625L3).

535 For long-exposure imaging, the laser intensity was attenuated significantly. Up to 2500
536 frames were collected per field-of-view with an exposure time of 500 ms.

537

538 **Long Exposure Data processing**

539 Broadly, image processing occurred in a two-step process. First, potential binding events
540 were identified using ThunderSTORM[59] generating regions of interest for further analysis.
541 Second, intensity traces over time were fitted with a Hidden Markov Model to distinguish
542 between a bound and background state.

Specifically, prior to PSF fitting, images from each field-of-view were background subtracted and cropped as needed. PSFs were fit using ThunderSTORM in ImageJ using the difference of Gaussians (DoG) filter option with a threshold of 1.5*std(Wave.F1)[59]. Candidate binding events were further narrowed down with a requirement for there to be a localization within 50 nm at least 2 times per 1000 frames. The image stack and its corresponding ThunderSTORM data was imported into MATLAB. Images were normalized and converted to photoelectron units. A simple nearest-neighbor linker associated detections across frames (distance threshold 300 nm; maximum frame gap 15) to form candidate bound trajectories.

For every frame within a trajectory, signal was quantified as the sum in a 5×5 pixel ROI centered on the trajectory position. Pooled photon values were modeled with a Gaussian mixture model (GMM; 3 components) to estimate background and signal intensity distributions. Per-track ROI time series were then segmented with a two-state hidden Markov model (HMM; background ↔ signal): initial state means/variances were set from the GMM, a conservative transition matrix was used and the most probable state sequence was decoded by Viterbi. Quality gates rejected traces with (i) peak intensity ≤ background upper bound, (ii) minimum intensity ≥ signal lower bound, (iii) dynamic range below the GMM-implied separation, or (iv) substantial signal/background standard-deviation overlap. Error codes were logged for each exclusion. In addition, any bound state event longer than 40 frames (20 seconds) was inspected and manually approved. Remaining signal segments were taken as valid dwell events; durations (frames) were converted to time using 0.5 s/frame and compiled across tracks.

Determination of t_{bound}

To characterize the distribution of bound state lifetimes, dwell time measurements were extracted for each condition and protein variant and binned into normalized histograms. To reduce the influence of short-duration events on the fit, the first histogram bin (0-0.5 seconds), a group that is disproportionally undercounted, was excluded from model fitting. For each distribution, both single- and double-exponential decay models were fitted to the data using nonlinear least-squares regression. The single-exponential model was defined as $\mathrm{y(t)} = \mathrm{A\,e^{-\lambda\,t}}$ and the double-exponential model as $y(t) = A_1 e^{-\lambda_1 t} + A_2 e^{-\lambda_2 t}$ with time constants $\tau_i = \frac{1}{\lambda_i}$.

Model selection was based on comparison of the Akaike Information Criterion (AIC), with the bi-exponential model favored if AIC was reduced by more than 2 units. In addition, if a state in the bi-exponential fit contributed less than 2% of the population, the mono-exponential model was favored. Goodness-of-fit was assessed via the coefficient of determination (R^2). For each fit, 99% confidence intervals were estimated by propagation of uncertainty using the Jacobian and parameter covariance matrix. Fits and their confidence intervals were overlaid on probability density plots to visualize lifetime distributions for each experimental condition.

Cluster detection and enrichment analysis

585 Single-molecule trajectories of SctQ, SctL, and SctN recorded under secretion-ON
586 conditions were analyzed to test whether long-lived binding events were spatially enriched.
587 Approved trajectories were converted into individual binding events, each represented by
588 the mean localization position and event duration. Events lasting ≥ 30 frames were
589 classified as long.

590 Spatial event clusters were identified using DBSCAN (ε = 100 nm, minPts = 2). For each
591 field of view, the observed fraction of long events within each cluster was compared with
592 the global fraction of long events using a one-sided hypergeometric test. Resulting p-
593 values were corrected for multiple testing by the Benjamini–Hochberg procedure (α =
594 0.05), and significant clusters were optionally validated by 2,000 random label-shuffle
595 permutations. Clusters were categorized as mixed, pure-long, or pure-short based on the
596 composition of event durations.

597

598 **Super-resolution fluorescence imaging & Data Processing**

599 Up to 20,000 frames are collected per field of view with an exposure time of 25 ms. Phase
600 contrast images were taken before and after fluorescence imaging. Raw data were
601 processed in MATLAB using a modified version of easy-DHPSF software[35,60]. Fluorescent
602 fiducial markers were used for sample drift correction. Phase contrast images were
603 segmented using Omnipose[61]. Single-molecule localizations were registered to phase
604 contrast masks using a two-step affine transformation in MATLAB, as described

605 previously[35]. Localizations outside of cells were discarded from further analysis using axial
606 bounds and Omnipose-derived cell outlines.

607

608 **MSD / cumulative displacement tracking**

609 To derive single-molecule displacements, localizations in subsequent frames were linked
610 into trajectories. A maximum linking distance of 2.5 μm was used for linking analysis, and
611 multiple localizations that were present at the same time within a single cell were
612 discarded to prevent misassignment of molecules.

613 For each trajectory, the cumulative displacement was calculated as the running sum of all
614 stepwise displacements between consecutive localizations,

621 $$CD_n = \sum_{i=2}^{n} \sqrt{(x_i - x_{i-1})^2 + (y_i - y_{i-1})^2 + (z_i - z_{i-1})^2}$$

615 where $x_i, y_i, z_i$are the 3D coordinates of the molecule at frame i. The cumulative
616 displacement versus time relationship was used to visualize overall molecular motion and
617 to compute the mean step size or slope of displacement accumulation over time. This
618 slope provided a direct, model-free metric of apparent mobility for each trajectory. The
619 plotted mean displacement normalized by time is thus an average of this displacement,
620 which is equivalent to the slope of the cumulative displacement curve over time.

622

623 **Estimating injectisome-bound fraction**

To identify the fraction of molecules bound, two parallel approaches were taken: RMS based classification of the trajectories, and clustering of the localizations to inform classifications of cluster-associated trajectories and non-associated trajectories. For RMS-based classification, trajectories were taken and the root mean squared radius was plotted. We recognized that injectisome associated trajectories display a very confined radius compared to cytosolic confusion (see Fig S4d). Trajectories could just be classified based on a threshold. For cluster-based classification, all localizations within one cell were taken and a clustering algorithm was applied. To avoid overcounting repeat localizations of the same molecule, trajectories were sorted based on association with a cluster or not.

<u>Spatial confinement–based classification of injectosome-bound trajectories</u>

Single-molecule trajectories were reconstructed as time-ordered 3D coordinates (x_i, y_i, z_i). For each trajectory, spatial confinement was quantified as the radius of gyration (RMS radius), defined as

$$R_{\mathrm{RMS}} = \sqrt{\frac{1}{M}\sum_{i=1}^{M}\left[(x_i - \bar{x})^2 + (y_i - \bar{y})^2 + (z_i - \bar{z})^2\right]},$$

where M is the number of localizations in the trajectory and $(\bar{x}, \bar{y}, \bar{z})$ is the centroid of that trajectory. Trajectories were classified as “injectosome-bound” if $R_{\mathrm{RMS}} < 120\mathrm{nm}$, and as “cytosolic/mobile” otherwise. For each cell, the fraction of injectosome-bound trajectories

643 was calculated and the percent bound value was reported as bound fraction representing
644 that cell's injectosome-association (table S5).

645

646 Detection of subcellular localization clusters

647 All 3D localizations (x, y, z) within a cell were clustered using density-based spatial
648 clustering (DBSCAN). Two parameters were defined per cell: (i) a spatial neighborhood
649 radius of 60 nm and (ii) a minimum cluster size (minPts). The minimum cluster size was
650 scaled with total localization count in that cell as minPts $=$ round$(N/300)$, where N is the
651 number of localizations in that cell, with a lower bound of 6 points. Cells for which this
652 procedure would have produced minPts ≤ 3 were excluded from cluster analysis.

653 Localizations that did not meet these density criteria were labeled as noise and not
654 assigned to a cluster. For each remaining cluster, the centroid was defined as the mean 3D
655 position of all localizations assigned to that cluster.

656 To determine whether a trajectory was spatially associated with an injectosome, each
657 trajectory from a given cell was compared to that cell's cluster centroids. For every
658 localization in a trajectory, the Euclidean distance to each centroid was computed, and the
659 minimum distance to the nearest centroid was retained.

660 A trajectory was classified as "injectosome-bound by proximity" if at least 50% of its
661 localizations lay within 100 nm of any cluster centroid. All other trajectories were classified
662 as unbound.

663 For every cell we therefore obtained: (i) the number of clusters detected, (ii) the percent
664 bound by cluster proximity, and (iii) the percent bound by RMS confinement. These per-cell
665 values were saved and then aggregated across fields of view, proteins, and conditions for
666 statistical comparisons (table S6).

667 **REFERENCES**

668 1 Galán, J. E. & Collmer, A. Type III Secretion Machines: Bacterial Devices for Protein
669 Delivery into Host Cells. *Science* **284**, 1322-1328 (1999).
670 https://doi.org/doi:10.1126/science.284.5418.1322
671 2 Hu, B., Lara-Tejero, M., Kong, Q., Galán, J. E. & Liu, J. In Situ Molecular Architecture
672 of the Salmonella Type III Secretion Machine. *Cell* **168**, 1065-1074.e1010 (2017).
673 https://doi.org/http://dx.doi.org/10.1016/j.cell.2017.02.022
674 3 Butan, C., Lara-Tejero, M., Li, W., Liu, J. & Galán, J. E. High-resolution view of the type
675 III secretion export apparatus in situ reveals membrane remodeling and a secretion
676 pathway. *Proc Natl Acad Sci U S A* **116**, 24786-24795 (2019).
677 https://doi.org/10.1073/pnas.1916331116
678 4 Kudryashev, M. *et al.* In situ structural analysis of the Yersinia enterocolitica
679 injectisome. *Elife* **2**, e00792 (2013). https://doi.org/10.7554/eLife.00792
680 5 Miletic, S. *et al.* Substrate-engaged type III secretion system structures reveal gating
681 mechanism for unfolded protein translocation. *Nat Commun* **12**, 1546 (2021).
682 https://doi.org/10.1038/s41467-021-21143-1
683 6 Torres-Vargas, C. *et al.* The inner rod of virulence-associated type III secretion
684 systems constitutes a needle adapter of one helical turn that is deeply integrated
685 into the system's export apparatus. *Molecular Microbiology* **112** (2019).
686 https://doi.org/10.1111/mmi.14327
687 7 Marcos-Vilchis, A. *et al.* On the role of the sorting platform in hierarchical type III
688 secretion regulation in enteropathogenic Escherichia coli. *Journal of Bacteriology*
689 **207** (2025). https://doi.org/10.1128/jb.00446-24
690 8 Mueller, C., Brož, P. & Cornelis, G. The type III secretion system tip complex and
691 translocon. *Molecular Microbiology* **68** (2008). https://doi.org/10.1111/j.1365-
692 2958.2008.06237.x
693 9 Takaya, A., Takeda, H., Tashiro, S., Kawashima, H. & Yamamoto, T. Chaperone-
694 mediated secretion switching from early to middle substrates in the type III
695 secretion system encoded by Salmonella pathogenicity island 2. *The Journal of*
696 *Biological Chemistry* **294**, 3783-3793 (2019).
697 https://doi.org/10.1074/jbc.ra118.005072
698 10 Wood, S., Jin, J. & Lloyd, S. YscP and YscU Switch the Substrate Specificity of the
699 Yersinia Type III Secretion System by Regulating Export of the Inner Rod Protein YscI.
700 *Journal of Bacteriology* **190**, 4252-4262 (2008). https://doi.org/10.1128/jb.00328-08
701 11 Cornelis, G. R. The Yersinia Ysc-Yop 'type III' weaponry. *Nat Rev Mol Cell Biol* **3**, 742-
702 752 (2002). https://doi.org/10.1038/nrm932
703 12 Dewoody, R. S., Merritt, P. M. & Marketon, M. M. Regulation of the Yersinia type III
704 secretion system: traffic control. *Front Cell Infect Microbiol* **3**, 4 (2013).
705 https://doi.org/10.3389/fcimb.2013.00004
706 13 Mehigh, R. J., Sample, A. K. & Brubaker, R. R. Expression of the low calcium
707 response in Yersinia pestis. *Microb Pathog* **6**, 203-217 (1989).
708 https://doi.org/10.1016/0882-4010(89)90070-3

14 Diepold, A. & Wagner, S. Assembly of the bacterial type III secretion machinery. *FEMS Microbiol Rev* **38**, 802-822 (2014). https://doi.org/10.1111/1574-6976.12061

15 Bergeron, J. R. C. & Marlovits, T. C. Cryo-EM of the injectisome and type III secretion systems. *Curr Opin Struct Biol* **75**, 102403 (2022). https://doi.org/10.1016/j.sbi.2022.102403

16 Hu, B. *et al*. Visualization of the type III secretion sorting platform of Shigella flexneri. *Proc Natl Acad Sci U S A* **112**, 1047-1052 (2015). https://doi.org/10.1073/pnas.1411610112

17 Makino, F. *et al*. The Architecture of the Cytoplasmic Region of Type III Secretion Systems. *Scientific Reports* **6**, 33341 (2016). https://doi.org/10.1038/srep33341

http://www.nature.com/articles/srep33341#supplementary-information

18 Berger, C. *et al*. Structure of the Yersinia injectisome in intracellular host cell phagosomes revealed by cryo FIB electron tomography. *Journal of Structural Biology* **213**, 107701 (2021). https://doi.org/https://doi.org/10.1016/j.jsb.2021.107701

19 Diepold, A. & Armitage, J. P. Type III secretion systems: the bacterial flagellum and the injectisome. *Philos Trans R Soc Lond B Biol Sci* **370** (2015). https://doi.org/10.1098/rstb.2015.0020

20 Bzymek, K. P., Hamaoka, B. Y. & Ghosh, P. Two translation products of Yersinia yscQ assemble to form a complex essential to type III secretion. *Biochemistry* **51**, 1669-1677 (2012). https://doi.org/10.1021/bi201792p

21 Yu, X. J., Liu, M., Matthews, S. & Holden, D. W. Tandem translation generates a chaperone for the Salmonella type III secretion system protein SsaQ. *J Biol Chem* **286**, 36098-36107 (2011). https://doi.org/10.1074/jbc.M111.278663

22 Jackson, M. W. & Plano, G. V. Interactions between type III secretion apparatus components from *Yersinia pestis* detected using the yeast two-hybrid system. *FEMS Microbiology Letters* **186**, 85-90 (2000). https://doi.org/10.1111/j.1574-6968.2000.tb09086.x

23 Morita-Ishihara, T. *et al*. Shigella Spa33 is an essential C-ring component of type III secretion machinery. *J Biol Chem* **281**, 599-607 (2006). https://doi.org/10.1074/jbc.M509644200

24 Spaeth, K. E., Chen, Y. S. & Valdivia, R. H. The Chlamydia type III secretion system C-ring engages a chaperone-effector protein complex. *PLoS Pathog* **5**, e1000579 (2009). https://doi.org/10.1371/journal.ppat.1000579

25 Soto, J. E., Galan, J. E. & Lara-Tejero, M. Assembly and architecture of the type III secretion sorting platform. *Proc Natl Acad Sci U S A* **119**, e2218010119 (2022). https://doi.org/10.1073/pnas.2218010119

26 Bernal, I. *et al*. Molecular Organization of Soluble Type III Secretion System Sorting Platform Complexes. *J Mol Biol* (2019). https://doi.org/10.1016/j.jmb.2019.07.004

27 Barison, N., Lambers, J., Hurwitz, R. & Kolbe, M. Interaction of MxiG with the cytosolic complex of the type III secretion system controls Shigella virulence. *FASEB J* **26**, 1717-1726 (2012). https://doi.org/10.1096/fj.11-197160

750 28 Wimmi, S. *et al.* Cytosolic sorting platform complexes shuttle type III secretion
751 system effectors to the injectisome in Yersinia enterocolitica. *Nat Microbiol* **9**, 185-
752 199 (2024). https://doi.org/10.1038/s41564-023-01545-1
753 29 Johnson, S. & Blocker, A. Characterization of soluble complexes of the Shigella
754 flexneri type III secretion system ATPase. *FEMS Microbiol Lett* **286**, 274-278 (2008).
755 https://doi.org/10.1111/j.1574-6968.2008.01284.x
756 30 Muthuramalingam, M. *et al.* The Structures of SctK and SctD from Pseudomonas
757 aeruginosa Reveal the Interface of the Type III Secretion System Basal Body and
758 Sorting Platform. *J Mol Biol* **432**, 166693 (2020).
759 https://doi.org/10.1016/j.jmb.2020.10.027
760 31 Galan, J. E., Lara-Tejero, M., Marlovits, T. C. & Wagner, S. Bacterial type III secretion
761 systems: specialized nanomachines for protein delivery into target cells. *Annu Rev*
762 *Microbiol* **68**, 415-438 (2014). https://doi.org/10.1146/annurev-micro-092412-
763 155725
764 32 Diepold, A. *et al.* A dynamic and adaptive network of cytosolic interactions governs
765 protein export by the T3SS injectisome. *Nat Commun* **8**, 15940 (2017).
766 https://doi.org/10.1038/ncomms15940
767 33 Lara-Tejero, M., Kato, J., Wagner, S., Liu, X. & Galan, J. E. A Sorting Platform
768 Determines the Order of Protein Secretion in Bacterial Type III Systems. *Science*
769 **331**, 1188-1191 (2011). https://doi.org/10.1126/science.1201476
770 34 Diepold, A., Kudryashev, M., Delalez, N. J., Berry, R. M. & Armitage, J. P.
771 Composition, formation, and regulation of the cytosolic c-ring, a dynamic
772 component of the type III secretion injectisome. *PLoS Biol* **13**, e1002039 (2015).
773 https://doi.org/10.1371/journal.pbio.1002039
774 35 Rocha, J. M. *et al.* Single-molecule tracking in live Yersinia enterocolitica reveals
775 distinct cytosolic complexes of injectisome subunits. *Integr Biol (Camb)* **10**, 502-
776 515 (2018). https://doi.org/10.1039/c8ib00075a
777 36 Prindle, J. R., Wang, Y., Rocha, J. M., Diepold, A. & Gahlmann, A. Distinct Cytosolic
778 Complexes Containing the Type III Secretion System ATPase Resolved by Three-
779 Dimensional Single-Molecule Tracking in Live Yersinia enterocolitica. *Microbiol*
780 *Spectr* **10**, e0174422 (2022). https://doi.org/10.1128/spectrum.01744-22
781 37 Pintor, K. *et al.* In situ analysis of type III secretion chaperone proteins indicates a
782 cytosolic handover of virulence effectors. *FEMS Microbes* **6**, xtaf010 (2025).
783 https://doi.org/10.1093/femsmc/xtaf010
784 38 Gilzer, D., Schreiner, M. & Niemann, H. H. Direct interaction of a chaperone-bound
785 type III secretion substrate with the export gate. *Nat Commun* **13**, 2858 (2022).
786 https://doi.org/10.1038/s41467-022-30487-1
787 39 Zhang, Y., Lara-Tejero, M., Bewersdorf, J. & Galan, J. E. Visualization and
788 characterization of individual type III protein secretion machines in live bacteria.
789 *Proc Natl Acad Sci U S A* **114**, 6098-6103 (2017).
790 https://doi.org/10.1073/pnas.1705823114
791 40 Akeda, Y. & Galan, J. E. Genetic Analysis of the Salmonella enterica Type III
792 Secretion-Associated ATPase InvC Defines Discrete Functional Domains. *Journal of*

Bacteriology **186**, 2402-2412 (2004). https://doi.org/10.1128/jb.186.8.2402-2412.2004

41 Nauth, T. *et al*. Visualization of translocons in Yersinia type III protein secretion machines during host cell infection. *PLoS Pathogens* **14** (2018). https://doi.org/10.1371/journal.ppat.1007527

42 Kudryashev, M. *et al*. Yersinia enterocolitica type III secretion injectisomes form regularly spaced clusters, which incorporate new machines upon activation. *Mol Microbiol* **95**, 875-884 (2015). https://doi.org/10.1111/mmi.12908

43 Grosdent, N., Maridonneau-Parini, I., Sory, M. P. & Cornelis, G. R. Role of Yops and adhesins in resistance of Yersinia enterocolitica to phagocytosis. *Infect Immun* **70**, 4165-4176 (2002). https://doi.org/10.1128/iai.70.8.4165-4176.2002

44 Navarro, L., Alto, N. M. & Dixon, J. E. Functions of the Yersinia effector proteins in inhibiting host immune responses. *Curr Opin Microbiol* **8**, 21-27 (2005). https://doi.org/10.1016/j.mib.2004.12.014

45 Galán, J. E. Common themes in the design and function of bacterial effectors. *Cell Host Microbe* **5**, 571-579 (2009). https://doi.org/10.1016/j.chom.2009.04.008

46 Zwack, E. E. *et al*. Inflammasome activation in response to the Yersinia type III secretion system requires hyperinjection of translocon proteins YopB and YopD. *mBio* **6**, e02095-02014 (2015). https://doi.org/10.1128/mBio.02095-14

47 Milne-Davies, B. *et al*. Life After Secretion-Yersinia enterocolitica Rapidly Toggles Effector Secretion and Can Resume Cell Division in Response to Changing External Conditions. *Front Microbiol* **10**, 2128 (2019). https://doi.org/10.3389/fmicb.2019.02128

48 Enninga, J., Mounier, J., Sansonetti, P. & Tran Van Nhieu, G. Secretion of type III effectors into host cells in real time. *Nat Methods* **2**, 959-965 (2005). https://doi.org/10.1038/nmeth804

49 Brianceau, C., Wimmi, S., Kronenberger, T. & Diepold, A. Continuous exchange of an inner-membrane ring component is required for assembly and function of the type III secretion system. *Nature Communications* **16**, 9889 (2025). https://doi.org/10.1038/s41467-025-65973-9

50 Prindle, J. R., de Cuba, O. I. C. & Gahlmann, A. Single-molecule tracking to determine the abundances and stoichiometries of freely-diffusing protein complexes in living cells: Past applications and future prospects. *J Chem Phys* **159** (2023). https://doi.org/10.1063/5.0155638

51 Diepold, A. *et al*. Deciphering the assembly of the Yersinia type III secretion injectisome. *EMBO J* **29**, 1928-1940 (2010). https://doi.org/10.1038/emboj.2010.84

52 Jouihri, N. *et al*. MxiK and MxiN interact with the Spa47 ATPase and are required for transit of the needle components MxiH and MxiI, but not of Ipa proteins, through the type III secretion apparatus of Shigella flexneri. *Molecular Microbiology* **49**, 755-767 (2004). https://doi.org/10.1046/j.1365-2958.2003.03590.x

53 Hueck, C. J. Type III Protein Secretion Systems in Bacterial Pathogens of Animals and Plants. *Microbiology and Molecular Biology Reviews* **62**, 379-433 (1998).

54 Majewski, D. D. *et al.* Cryo-EM structure of the homohexameric T3SS ATPase-central stalk complex reveals rotary ATPase-like asymmetry. *Nature Communications* **10**, 626 (2019). https://doi.org/10.1038/s41467-019-08477-7

55 Schlumberger, M. C. *et al.* Real-time imaging of type III secretion: Salmonella SipA injection into host cells. *Proceedings of the National Academy of Sciences* **102**, 12548-12553 (2005). https://doi.org/doi:10.1073/pnas.0503407102

56 Rocha, J., Corbitt, J., Yan, T., Richardson, C. & Gahlmann, A. Resolving Cytosolic Diffusive States in Bacteria by Single-Molecule Tracking. *Biophys J* **116**, 1970-1983 (2019). https://doi.org/10.1016/j.bpj.2019.03.039

57 Pavani, S. R. P. *et al.* Three-dimensional, single-molecule fluorescence imaging beyond the diffraction limit by using a double-helix point spread function. *Proceedings of the National Academy of Sciences of the United States of America* **106**, 2995-2999 (2009). https://doi.org/10.1073/pnas.0900245106

58 Thompson, M. A., Lew, M. D., Badieirostami, M. & Moerner, W. E. Localizing and tracking single nanoscale emitters in three dimensions with high spatiotemporal resolution using a double-helix point spread function. *Nano Letters* **10**, 211-218 (2010). https://doi.org/10.1021/nl903295p

59 Ovesny, M., Krizek, P., Borkovec, J., Svindrych, Z. & Hagen, G. M. ThunderSTORM: a comprehensive ImageJ plug-in for PALM and STORM data analysis and super-resolution imaging. *Bioinformatics* **30**, 2389-2390 (2014). https://doi.org/10.1093/bioinformatics/btu202

60 Lew, M. D., von Diezmann, A. R. S. & Moerner, W. E. Easy-DHPSF open-source software for three-dimensional localization of single molecules with precision beyond the optical diffraction limit. *Protocol Exchange*, doi:10.1038/protex.2013.1026 (2013). https://doi.org/doi:10.1038/protex.2013.026

61 Cutler, K. J. *et al.* Omnipose: a high-precision morphology-independent solution for bacterial cell segmentation. *Nat Methods* **19**, 1438-1448 (2022). https://doi.org/10.1038/s41592-022-01639-4